

## **Raman Lidar (RL) Instrument Handbook**

RK Newsom  
D Chand

R Bambha

December 2022



## **DISCLAIMER**

This report was prepared as an account of work sponsored by the U.S. Government. Neither the United States nor any agency thereof, nor any of their employees, makes any warranty, express or implied, or assumes any legal liability or responsibility for the accuracy, completeness, or usefulness of any information, apparatus, product, or process disclosed, or represents that its use would not infringe privately owned rights. Reference herein to any specific commercial product, process, or service by trade name, trademark, manufacturer, or otherwise, does not necessarily constitute or imply its endorsement, recommendation, or favoring by the U.S. Government or any agency thereof. The views and opinions of authors expressed herein do not necessarily state or reflect those of the U.S. Government or any agency thereof.

# **Raman Lidar (RL) Instrument Handbook**

RK Newsom, Pacific Northwest National Laboratory (PNNL)  
R Bambha, Sandia National Laboratories  
D Chand, PNNL

December 2022

How to cite this document:

Newsome, RK, R Bambha, and D Chand. 2022. Raman Lidar (RL) Instrument Handbook. U.S. Department of Energy, Atmospheric Radiation Measurement user facility, Richland, Washington. DOE/SC-ARM-TR-038.

Work supported by the U.S. Department of Energy,  
Office of Science, Office of Biological and Environmental Research

## Acronyms and Abbreviations

ADC	ARM Data Center
AGL	above ground level
AMF	ARM Mobile Facility
ANSI	American National Standards Institute
ARM	Atmospheric Radiation Measurement
ARRA	American Recovery and Reinvestment Act
CF	Central Facility
CONUS	continental United States
Copol	copolarization (i.e., parallel to transmit polarization)
DBS	dichroic beam splitter
depol	depolarization (i.e., perpendicular to transmit polarization)
DOE	U.S. Department of Energy
ENA	Eastern North Atlantic
FEX	feature extraction and extinction
FOV	field of view
FWHM	full width at half maximum
HVAC	heating, ventilation, and air conditioning
MPE	maximum permissible exposure
NFOV	narrow field of view
PBS	polarizing beam splitter
PMT	photomultiplier tube
PNNL	Pacific Northwest National Laboratory
RF	radio frequency
RL	Raman lidar
SDS	site data system
SGP	Southern Great Plains
SGPC1	Southern Great Plains Central Facility
SGPRL	Southern Great Plains Raman lidar
TWP	Tropical Western Pacific
unpol	unpolarized
UTC	Coordinated Universal Time
UV	ultraviolet
VAC	volts alternating current
VAP	value-added product
WFOV	wide field of view
WVMR	water vapor mixing ratio

# Contents

Acronyms and Abbreviations .....	iii
1.0 General Overview .....	1
2.0 Contacts .....	1
3.0 Deployment Locations and History .....	2
3.1 RL01 .....	2
3.2 RL02 .....	5
3.3 RL03 .....	7
4.0 Instrument Description .....	8
4.1 Theory of Operation .....	8
4.2 System Specifications .....	9
4.3 Eye Safety .....	12
4.4 Calibration .....	12
5.0 Data Description .....	13
5.1 Raw Data Collection and Ingest .....	13
5.2 Raw Data File Contents .....	13
5.3 Measurement Uncertainty .....	15
5.4 Value-Added Products .....	15
5.5 Annotated Examples .....	16
6.0 References .....	22

## Figures

1	SGP C1 layout showing past and current locations of the RL. ....	3
2	RL01 at SGP C1 a) before October 2015, and b) after January 2016. ....	4
3	The hatch, window, and hail shield for the RL01. ....	4
4	Uptime for the RL01 during the first ~13 years of operation. ....	5
5	Daily Uptime for the RL01 from January 2009 through December 2020. ....	5
6	Locations for the RL02 at a) TWP C3 from 2010 to 2015, and b) ENA C1 from 2015 to the present. ....	6
7	The RL02 at a) TWP C3, and at b) ENA C1. ....	6
8	Uptime for the RL02 during its time at the TWP C3 site. ....	7
9	Uptime for the RL02 at ENA C1. ....	7
10	a) Aerial view of the Oliktok site showing the location of the RL03. b) Ground-level view of the RL03 with other instrumentation at the Oliktok site. ....	7
11	Instrument uptime for the RL03 during its deployment with the AMF3 in Oliktok Point, Alaska. ....	8
12	Layout of the lidar enclosure as viewed from above. ....	9
13	Schematic of the ARM RL receiver. ....	10
14	SGPRL VAP flow diagram. ....	16
15	Profiles of a) NFOV copol, and b) NFOV N <sub>2</sub> . ....	17
16	Sample time-height display of the NFOV Depol signals showing a) photon counts, and b) analog voltages. ....	18
17	Sample time-height display of the NFOV Copol signals showing a) photon counts, and b) analog voltages. ....	18
18	Sample time-height display of the NFOV N <sub>2</sub> signals showing a) photon counts, and b) analog voltages. ....	19
19	Sample time-height display of the NFOV H <sub>2</sub> O signals showing a) photon counts, and b) analog voltages. ....	19
20	Sample time-height display of the NFOV RR1 signals showing a) photon counts, and b) analog voltages. ....	20
21	Sample time-height display of the NFOV RR2 signals showing a) photon counts, and b) analog voltages. ....	20
22	Comparison of the a) NFOV and b) WFOV photon counting signal for N <sub>2</sub> . ....	21
23	Comparison of the a) NFOV and b) WFOV photon counting signals for H <sub>2</sub> O. ....	21

## Tables

1	Locations of the ARM Raman lidars.....	2
2	Peak wavelengths ( $\lambda_{\text{peak}}$ ), peak transmissions ( $\tau_{\text{peak}}$ ), and bandwidths (FWHM) for the interference filters used in the ARM RL’s detection channels. All interference filters used by the ARM RLs are manufactured by Barr Associates Inc. ....	11
3	ARM Raman lidar specifications. ....	11
4	Primary variables <site>rl<facility>.a0 datastream. Photon counts and analog voltages are stored as 2-dimensional arrays, where the two dimensions are time and height.....	13
5	Secondary variables in the <site>rl<facility>.a0 datastream. ....	14
6	Engineering and diagnostic variables in the raw RL datastream that provide information on the health of the system.....	15
7	Current RL value-added products. ....	16

## 1.0 General Overview

The Raman lidars (RL) operated by the U.S. Department of Energy (DOE) Atmospheric Radiation Measurement (ARM) user facility are semi-autonomous, land-based, laser remote-sensing systems that provide height- and time-resolved measurements of atmospheric water vapor mixing ratio, temperature, aerosol backscatter, extinction, and linear depolarization ratio from about 200m to greater than 10km AGL.

The RL operates by transmitting short pulses of ultraviolet (UV) laser light (at 355 nm) into the atmosphere and recording the resultant backscatter as a function of time. Ranging information is obtained by converting the time axis to distance using the speed of light. As the laser pulse propagates through the atmosphere, its energy is scattered by aerosols and molecules, and a small fraction of the incident energy is returned to the receiver. For a given transmit wavelength, each molecule exhibits a unique Raman spectrum. This property is used to estimate the mixing ratio of targeted species.

The ARM RLs use separate detection channels to measure the elastic backscatter at 355 nm, as well as Raman backscatter from atmospheric H<sub>2</sub>O at 408 nm, and N<sub>2</sub> at 387 nm. Water vapor mixing ratio is estimated from the ratio of the H<sub>2</sub>O and N<sub>2</sub> return signals. Aerosol properties such as the backscatter coefficient and extinction are estimated from the elastic and N<sub>2</sub> returns, and temperature estimates are obtained from measurements of the rotational Raman spectrum near the transmit wavelength.

The ARM RLs are housed inside environmentally controlled shipping containers. The main components of the lidar system include the laser transmitter, the telescope, the receiving optics and detectors, data acquisition system, and associate electronics. The systems are designed to operate 24 hours a day, 7 days a week in an autonomous mode.

The ARM facility currently operates three Raman lidar (RL) systems. Two of these systems are deployed at the Southern Great Plains (SGP) site, and at the Eastern North Atlantic (ENA) site. The third system was previously deployed with the third ARM Mobile Facility (AMF3) at Oliktok Point, Alaska. That system will ultimately be redeployed somewhere in the southeast continental United States (CONUS).

## 2.0 Contacts

Rob Newsom  
Pacific Northwest National Laboratories  
P.O. Box 999, MSIN K9-30  
Richland, Washington 99352  
Phone: 509-372-6020  
Fax: 509-372-6168  
rob.newsom@pnl.gov

Ray Bamba (engineering)  
Sandia National Laboratories  
[jgold@sandia.gov](mailto:jgold@sandia.gov)

### 3.0 Deployment Locations and History

The ARM facility (Mather and Voyles 2013) currently operates Raman lidars at the SGP and ENA sites, and the third ARM Mobile Facility (AMF3). Table 1 lists the locations and deployment dates for each of the three systems. We refer to these systems as RL01, RL02, and RL03, where the numbers indicate the order in which the systems were developed.

**Table 1.** Locations of the ARM Raman lidars.

System	Site and Facility	Latitude	Longitude	Dates	
				Start	End
RL01	SGP C1	36.605277°	-97.486625°	201601	Present
	SGP C1	36.607906°	-97.487125°	199608	201510
RL02	TWP C3	39.091177°	-28.026825°	201012	201501
	ENA C1	-12.424547°	130.89153°	201509	Present
RL03	SEUS	TBD	TBD	TBD	
	OLI M1	70.494856°	-149.88647°	201410	202101

#### 3.1 RL01

In the early 1990s ARM funded a collaboration between Sandia National Laboratories and the National Aeronautics and Space Administration Goddard Space Flight Center to pursue technology improvements that would meet ARM’s requirements for ground-based remote sensing of water vapor. That effort ultimately led to the development of ARM’s first Raman lidar, which was initially deployed in the summer of 1996 at ARM’s SGP C1 site (also known as the SGP Central Facility [CF]).

The original SGP RL (prior to 2004) had seven detection channels and used photon-counting electronics, as described by Goldsmith et al. 1998. During the first few years of its deployment, value-added products (VAPs) were developed to generate geophysical parameters from the raw photon counting data (Turner et al. 1999, 2000, 2002, Ferrare et al. 2006). These data products include water vapor mixing ratio, relative humidity, aerosol scattering ratio, aerosol backscatter, aerosol extinction, aerosol optical depth, aerosol depolarization ratio, and cloud base height. Turner et al. (2016) provides an excellent overview of the first 20 years of the operation of the RL01.

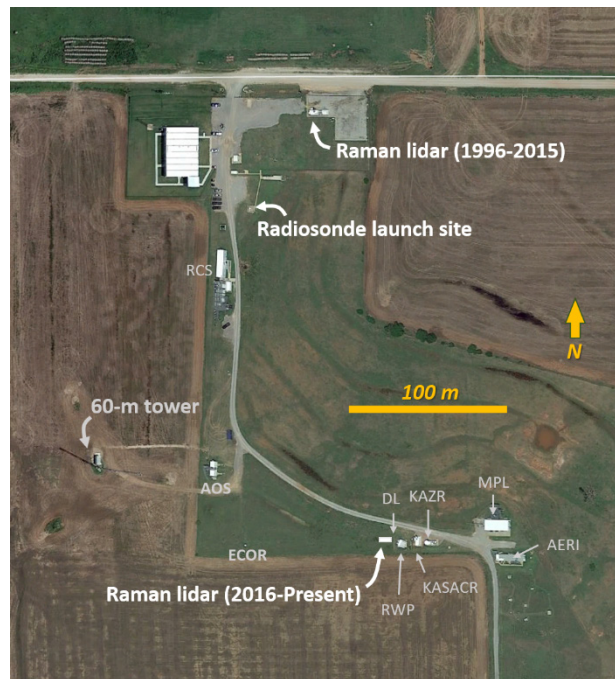
The RL01 underwent a major refurbishment in 2004, following a period of degraded sensitivity (Turner and Goldsmith 2005). During the refurbishment the primary telescope was resurfaced, optical components and filters were replaced, and the existing photon-counting electronics were replaced with new Licel transient data recorders. The Licel recorders interface with the photomultiplier tubes (PMTs) to provide simultaneous measurements of both analog voltage and photon counts. Merging these two signals enabled a significant improvement in the dynamic range of the measurements (Whiteman et al. 2006, Newsom et al 2009). The new Licel data recorders also enabled a significant improvement in the range resolution of the raw data. Prior to the refurbishment in 2004 the range resolution was 39 m; after the installation of the Licel recorders the range resolution was set to 7.5 m.

In October 2005, three new detection channels were added to RL01 to enable profiling of temperature and liquid water content. Although the current system retains the two temperature channels, the liquid water channel is no longer supported. Also, the alignment stability of the system was improved with addition of a boresight alignment module in April 2007.

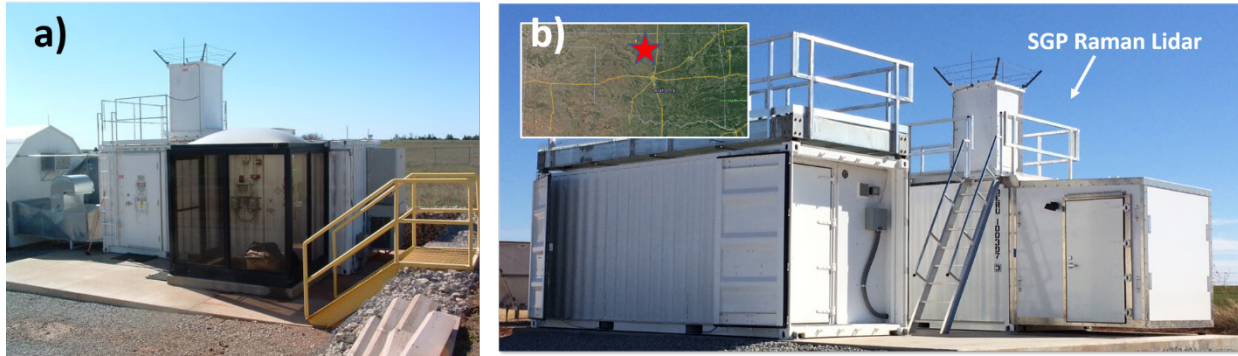
The RL01 underwent another round of upgrades in late 2015 in which the entire lidar was reinstalled inside a new container with a new computer-controlled proportional-response HVAC system, providing improved temperature stability. Also a new transmit beam-steering system was added, and the entire system was moved about 300 m to the south of its original location, as shown in Figure 1. Originally, the system was located near the northern boundary of the site. In 2015 it was moved south to be collocated with a Doppler lidar and several radar systems.

Figure 2 shows the RL01 before and after the move in 2015. Prior to the move, the RL01 used a double entry system (also known as the “bus stop”) as an added safety feature and to help keep particulate concentrations down inside the enclosure. This feature was deemed unnecessary and was not retained after the system was moved.

Laser light exits through a hatch in the top of the lidar enclosure. The hatch is surrounded by a light baffle that protrudes from the top of the enclosure, as seen in Figure 2. Figure 3 shows the hatch and window assembly. Since the RL01 operates in Tornado Alley, the window assembly includes a metal shield that is intended to protect the window from hail damage. We note that the other ARM RLs do not use hail shields.



**Figure 1.** SGP C1 layout showing past and current locations of the RL. Locations of several other instruments, including the radiosonde launch site, are also shown.



**Figure 2.** RL01 at SGP C1 a) before October 2015, and b) after January 2016.

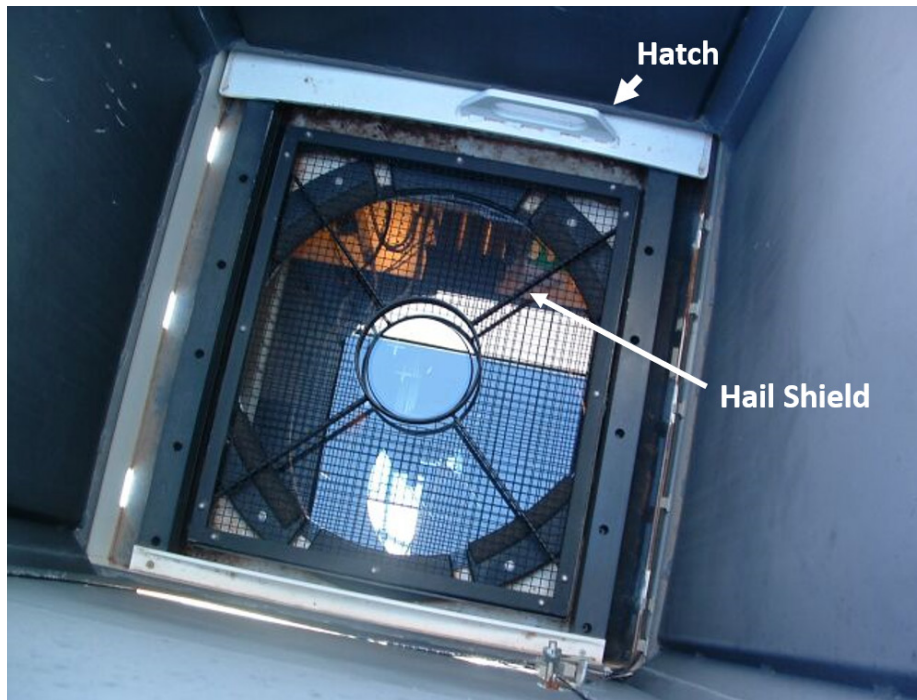


**Figure 3.** The hatch, window, and hail shield for the RL01. The view is from above, looking down the light baffle. The shield is designed to allow the passage of the transmit beam, while protecting most of the remaining window area from hail.

Figure 4 shows monthly uptime statistics for the RL01 from 1996 until the beginning of 2009. Here we define uptime as the percentage of time the system is operational and producing data. During the first several years of operation the uptime increased as design improvements were implemented and as the onsite staff improved their familiarity with the system. Daily uptime for the period from January 2009 through December 2020 is shown in Figure 5. The average uptime during this period was approximately 90%. Major periods of instrument downtime occurred in the fall of 2011, the fall and winter of 2015 (due to the move), early and late 2018, and in the spring of 2020 due to the COVID-19 pandemic.

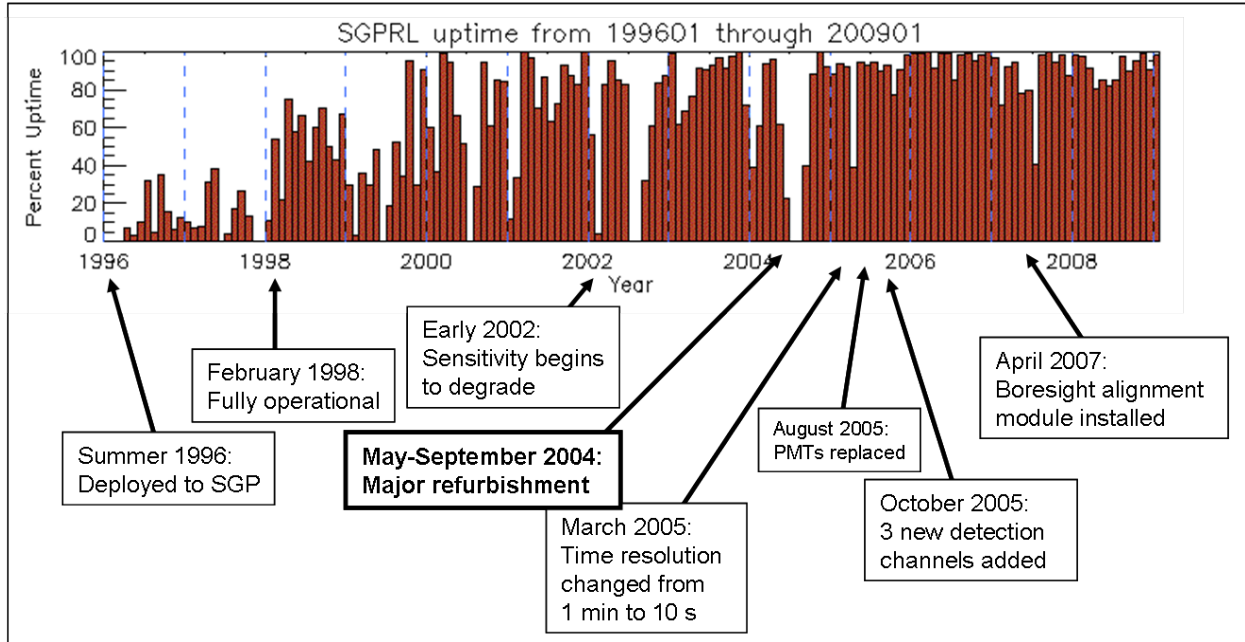


**Figure 4.** Uptime for the RL01 during the first ~13 years of operation.

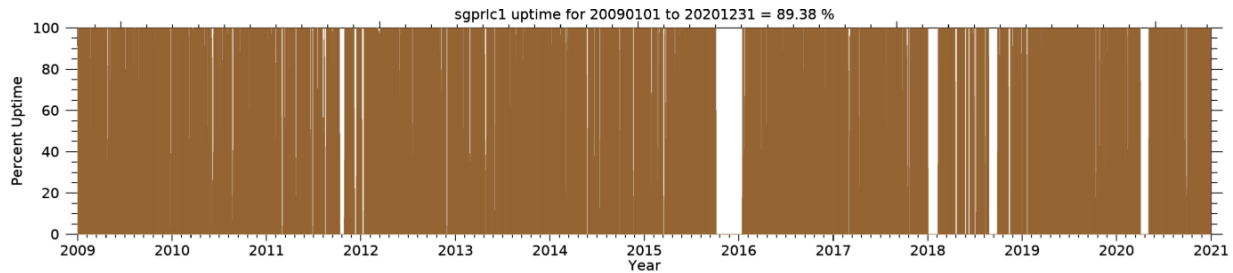


**Figure 5.** Daily uptime for the RL01 from January 2009 through December 2020.

### 3.2 RL02

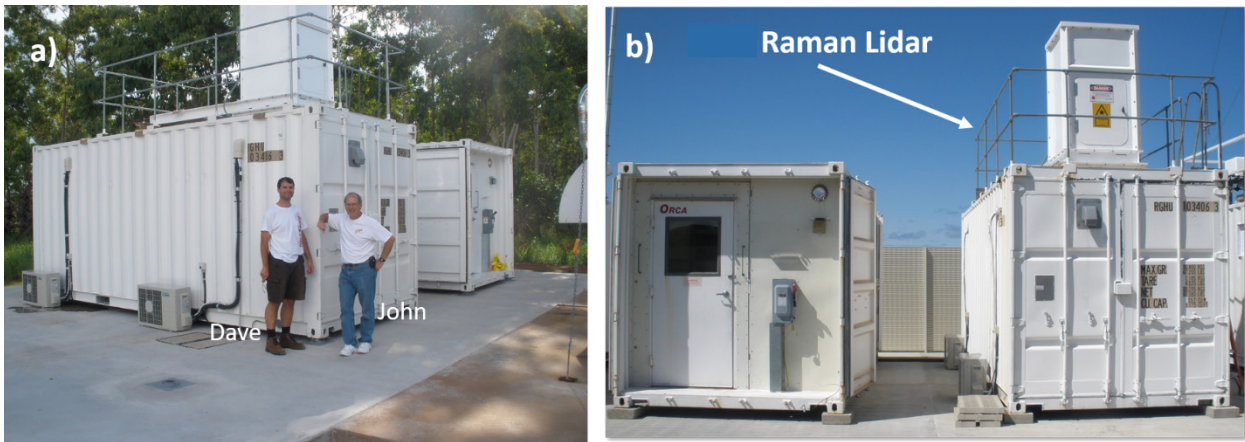
Development of the second ARM Raman lidar (RL02) began in 2009 with funding from the American Recovery and Reinvestment Act (ARRA). To reduce risk and ensure timely delivery, the design of the new system closely followed that of the existing SGP Raman lidar (RL01).

Figure 6 shows the deployment locations for the RL02. Initially the system was deployed at the Tropical Western Pacific (TWP) site in Darwin, Australia (-12.425°, 130.892°) in December 2010, where it operated until the TWP site was decommissioned in January 2015. The system was then relocated to the ENA C1 site (39.091°, -28.027°) on Graciosa Island in the Azores, where it has been operating since September 2015.

Figure 7 shows the RL02 at TWP and at ENA. Although the design and operation of the RL02 system is similar to the RL01, there are a few minor differences. First, the RL02 was never fitted with a hail shield as this was deemed unnecessary for Darwin. Second, due to the high solar angle at Darwin during portions of the year, the hatch was programmed to close when the solar angle was within ~27° of zenith to prevent damage to the PMTs from prolonged exposure to solar radiation.



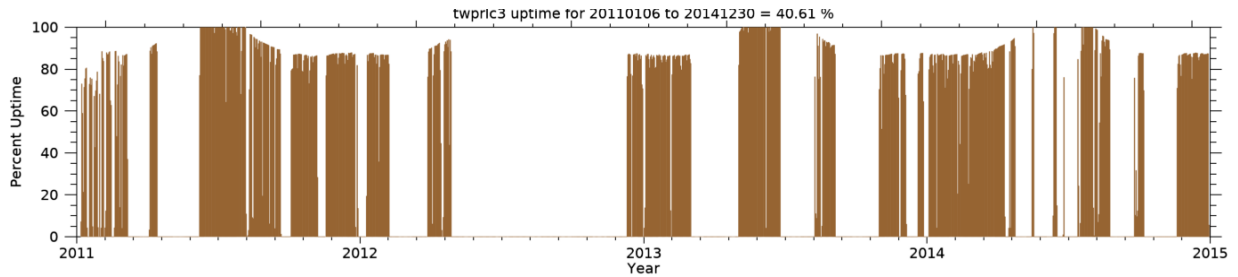
**Figure 6.** Locations for the RL02 at a) TWP C3 from 2010 to 2015, and b) ENA C1 from 2015 to the present. The TWP C3 site was located just south of the Darwin Airport runway. The ENA C1 site is located near the main terminal of the Graciosa Airport.



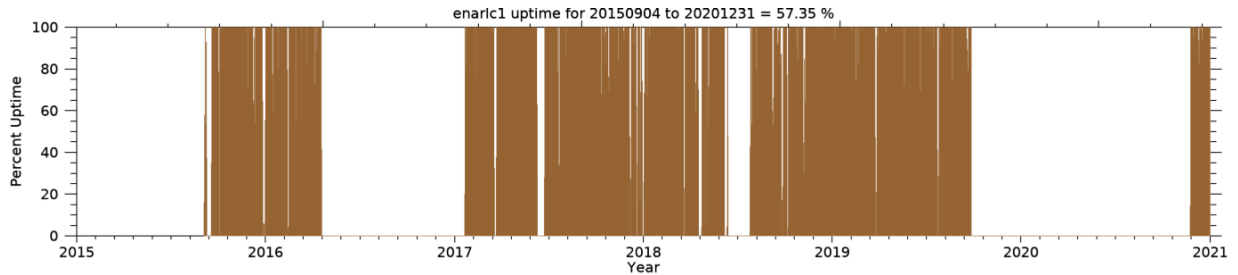
**Figure 7.** The RL02 at a) TWP C3, and at b) ENA C1.

Figure 8 shows daily uptime statistics for the RL02 during its time in Darwin. The average uptime during this period was about 41%. This figure also clearly shows the reduction in daily uptime associated with the closing of the hatch during periods with high solar angles.

Figure 9 shows daily uptime statistics for the RL02 during its deployment at ENA C1 on Graciosa Island. This uptime covers the period from its initial installation in September 2015 to the end of 2020. The average uptime during this period was about 57%. The system experienced its longest period of downtime from the fall of 2019 until November 2020. Travel restrictions that were put in place during the COVID-19 pandemic led to significant delay in repair of the system.



**Figure 8.** Uptime for the RL02 during its time at the TWP C3 site. The uptime during this period was about 40%.



**Figure 9.** Uptime for the RL02 at ENA C1. The uptime during this period was about 57%.

### 3.3 RL03

Sandia National Laboratory began development of a third Raman lidar in 2013, closely following the design of the previous two systems. The RL03 was first deployed with the new 3rd ARM Mobile Facility (AMF3) at Oliktok Point, Alaska, as shown in Figure 10. The system operated (intermittently) at this site from September 2014 until early 2021. The current plan is for this system to be moved, together with other instruments, to a new fixed site to be established in the southeast U.S.

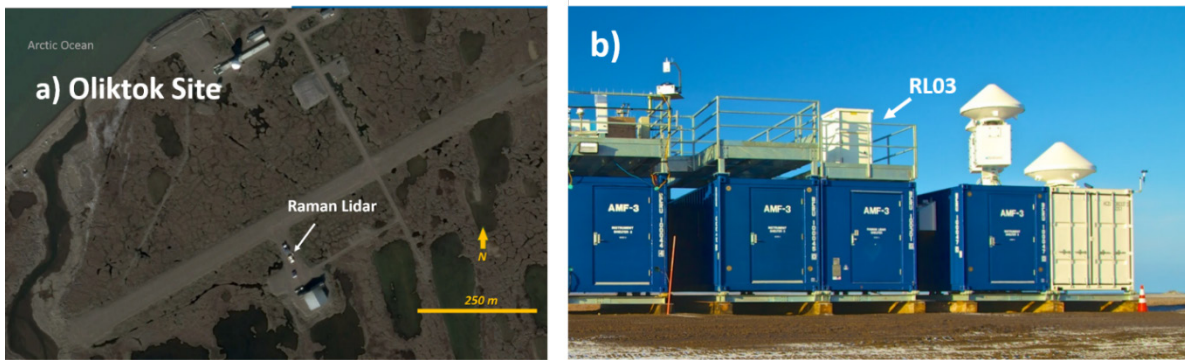


**Figure 10.** a) Aerial view of the Oliktok site showing the location of the RL03. b) Ground-level view of the RL03 with other instrumentation at the Oliktok site.

Operating a Raman lidar at a remote arctic location proved to be a challenge. Figure 11 shows the percent uptime of the RL03 during its deployment with AMF3. As indicated, this system operated intermittently with only about 26% uptime during the entire period. The low uptime is largely a result of logistical challenges associated with getting equipment and qualified service personnel to and from the remote site. Power reliability was also an issue.

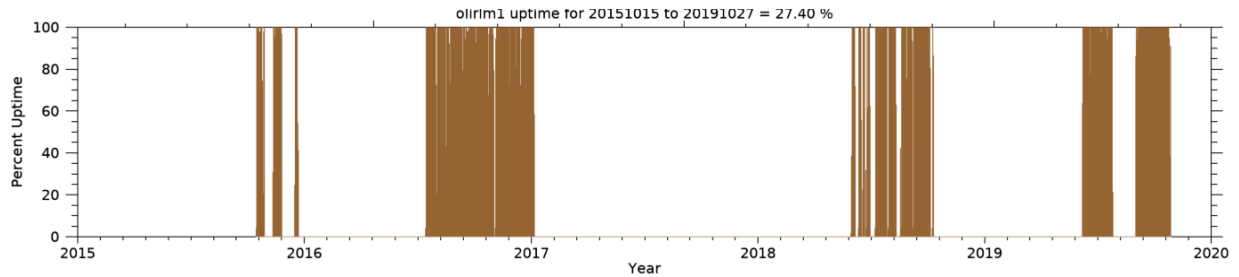


**Figure 11.** Instrument uptime for the RL03 during its deployment with the AMF3 in Oliktok Point, Alaska. The total uptime from first light to final shutdown was about 27%.

## 4.0 Instrument Description

In this section we describe the theory of operation, hardware specifications, eye safety, and calibration of the ARM Raman lidars.

### 4.1 Theory of Operation

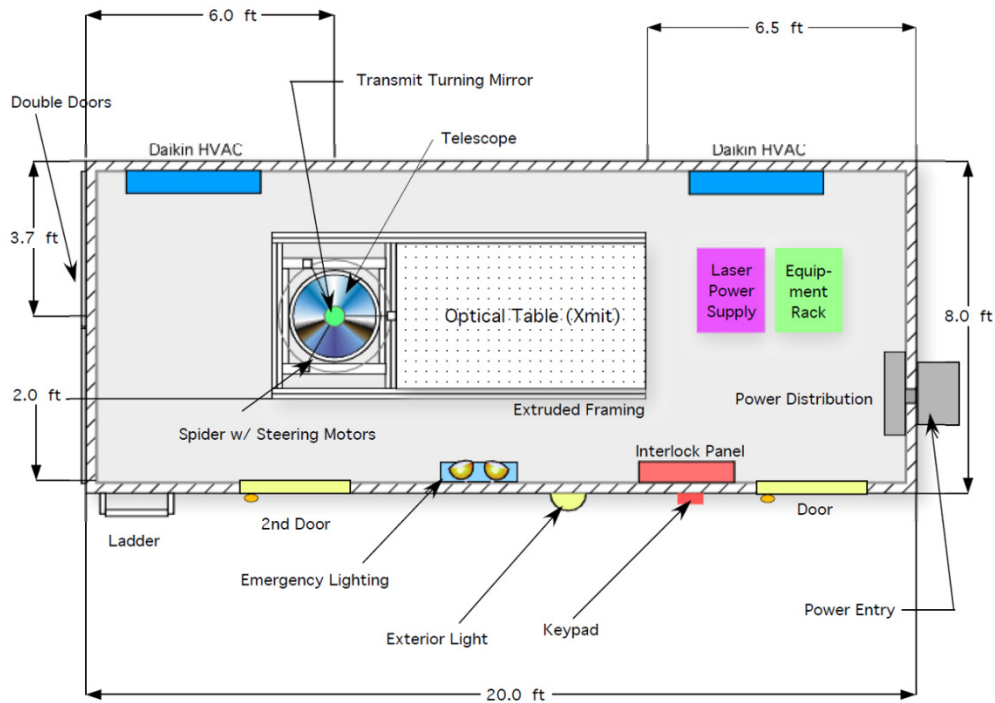
The ARM Raman lidars operate by transmitting short pulses of UV light (355 nm) into the atmosphere and recording the resultant return or ‘echo’ signal as a function of time. The time axis is converted to range using the speed of light. As the transmitted laser pulse travels through the atmosphere it induces vibrational and rotational transitions in molecular H<sub>2</sub>O, N<sub>2</sub>, and O<sub>2</sub> that lead to re-emission at other wavelengths via the Raman effect (Raman 1928). The return signal at the transmit wavelength (355 nm) contains a strong elastically scattered contribution from clouds and aerosols with a smaller contribution from molecular Rayleigh scattering. Contributions from Raman backscatter at other wavelengths are quite a bit smaller than the elastic returns. The ARM RLs use narrowband detection techniques to measure these relatively weak Raman signals.

Separate detection channels are used for measurement of the elastic and Raman return signals. Raman backscatter from H<sub>2</sub>O is measured at 408 nm, and Raman backscatter from N<sub>2</sub> is measured at 387 nm. The elastic and N<sub>2</sub> signals are used to derive the aerosol optical properties generated by the Feature extraction and Extinction (FEX) VAP (Chand et al. 2020, Thorsen et al. 2015a, 2015b). The H<sub>2</sub>O and N<sub>2</sub> signals are used to derive water vapor mixing ratio (Whiteman et al. 1992, Turner et al. 1999, 2000, 2002, Ferrare et al. 2006, Whiteman et al. 2006). Additionally, two detection channels measure the energy content in two different portions of the rotational Raman spectra of N<sub>2</sub> and O<sub>2</sub>. These channels are used to derive temperature, as described in Newsom et al. 2013 and 2018.

The RL detection system also incorporates a narrow and a wide field of view (FOV). The narrow FOV provides good discrimination of the weak Raman backscatter signal above the background in the far field, while the wide FOV enables detection at closer range. The narrow field of view, coupled with the use of narrowband filters, reduces the background skylight and, therefore, increases the maximum range for derived parameters (e.g., water vapor mixing ratio) during the daytime.

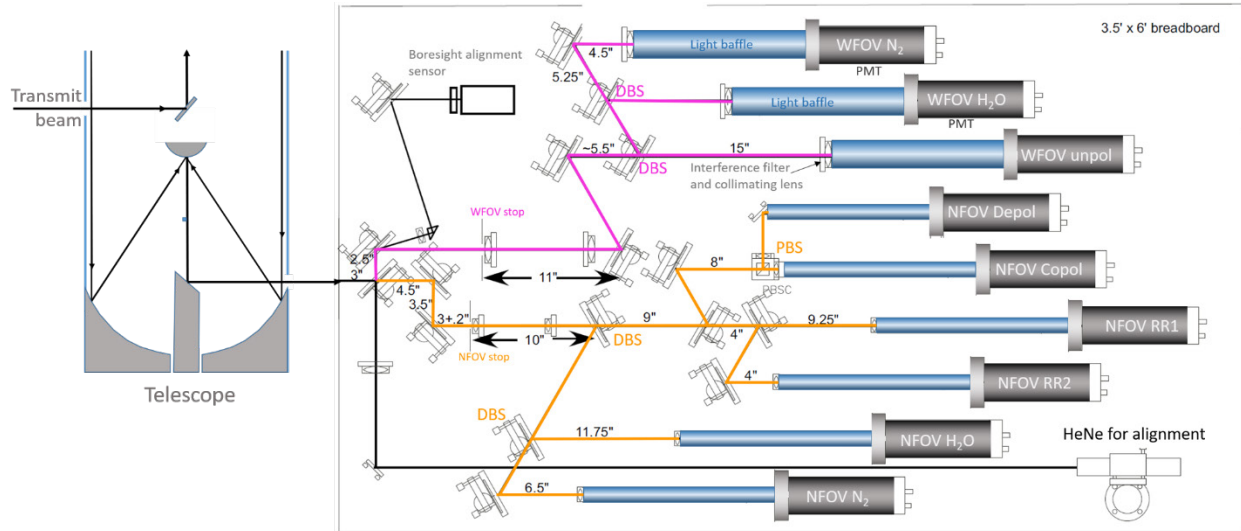
## 4.2 System Specifications

Figure 12 shows the layout of the major subsystems inside the lidar enclosure. The enclosure itself is a modified standard metal shipping container with outside dimensions of approximately 2.4 m high by 2.4 m wide by 6.1 m long. Major subsystems shown in Figure 12 include the HVAC system, the optical table and telescope assembly, the laser power supply, and an equipment rack for the data system and detector power supplies. The entire system, including the lidar, weighs approximately 5000 kg and the nominal power draw of the entire system is 14400VA (60 A @ 240 VAC).



**Figure 12.** Layout of the lidar enclosure as viewed from above.

The RL transmitter consists of a frequency-tripled Nd:YAG manufactured by Continuum Inc. The fundamental wavelength of the Nd:YAG gain medium is 1064 nm. Output at 355 nm is achieved through third harmonic generation in which the frequency of the output light is tripled. Pulse formation is achieved by q-switching the laser cavity using an external trigger signal from a pulse generator. The laser is configured to output 5ns pulses at a repetition frequency of 30 Hz, and a nominal pulse energy of 300mJ. The output of the laser, which is linearly polarized, is then passed through a beam-expanding telescope to increase the beam diameter to 13 cm. The beam expander also reduces the beam divergence to 0.1 mrad, thereby permitting the use of a narrow (0.3 mrad) as well as a wide (2 mrad) field of view. After expansion, the beam is directed out of the enclosure through a hatch and window assembly in the roof. The window material is high-optical-quality uncoated plate glass, with a thickness of 6.3 mm and a diameter of 69 cm.



**Figure 13.** Schematic of the ARM RL receiver. The atmospheric return signal is collected by the telescope and then directed into the receiver where it is split between a narrow FOV (NFOV) path (orange) and a wide FOV (WFOV) path (violet).

Figure 13 shows the layout of the RL receiver. A 61-cm-diameter telescope collects the light backscattered from the atmosphere. The receiver uses all free space coupled optics and contains a total of nine detection channels. Light entering the receiver is first split by a wedged beam splitter into narrow FOV (NFOV) and wide FOV (WFOV) paths. Dichroic beam splitters separate the light by wavelength to improve detection at the elastic and Raman wavelengths. These signals are directed into photomultiplier tubes (Electron Tubes 9954B). All PMT are fitted with light baffles (aluminum tubes), with interference filters and collimating lenses mounted at the entrances. The filters and dichroic beam splitters enable very narrow band detection and good suppression of the background. The outputs from the PMTs are acquired by Licel data recorders, which are configured to output both photon counts and analog voltages with a time resolution of 10 s and a range resolution of 7.5 meters.

As indicated in Figure 13, the WFOV path contains three detection channels, and the NFOV path contains six channels. There are a total of three elastic channels, including one WFOV channel that is not sensitive to polarization, and two NFOV channels that are polarization sensitive. A polarizing beam splitter (labeled “PBS” in Figure 13) separates the light into two orthogonal linear polarizations. The “copol” channel measures the elastic backscatter with polarization parallel to the outgoing beam, and the “depol” channel measures the elastic backscatter with polarization perpendicular to the outgoing beam.

A boresight alignment module is also shown in Figure 13. The alignment module monitors the position of the laser spot in the receiver’s field of view and uses that information to continually adjust the steering of the outgoing beam to maintain optimal alignment with the receiver telescope.

Table 2 lists the center wavelengths and FWHM values of the interference filters used in each of the detection channels, and Table 3 summarizes the major specifications of the ARM Raman lidar systems.

**Table 2.** Peak wavelengths ( $\lambda_{\text{peak}}$ ), peak transmissions ( $\tau_{\text{peak}}$ ), and bandwidths (FWHM) for the interference filters used in the ARM RL’s detection channels. All interference filters used by the ARM RLs are manufactured by Barr Associates Inc.

Detection Channel	$\lambda_{\text{peak}}$ (nm)	$\tau_{\text{peak}}$ (%)	FWHM (nm)
WFOV unpol	354.70	57	0.30
WFOV N <sub>2</sub>	386.70	58	0.31
WFOV H <sub>2</sub> O	407.45	55	0.28
NFOV copol	354.68	58	0.30
NFOV depol	354.68	58	0.30
NFOV N <sub>2</sub>	386.69	70	0.30
NFOV H <sub>2</sub> O	407.46	70	0.26
NFOV RR1 (low-J)	354.27	34	0.22
NFOV RR2 (high-J)	353.27	37	0.20

**Table 3.** ARM Raman lidar specifications.

Lidar Enclosure	
Manufacturer	Orca
total weight	~11000 lbs
lidar power requirement	240 VAC single phase @ 10 A
HVAC manufacturer	Daikin
HVAC power requirement	240 VAC single phase @ 50 A
Transmitter	
Laser/manufacture	frequency-tripled Nd:YAG/Continuum
Output wavelength	355 nm
Pulse generator manufacturer	Stanford Research Systems
Pulse energy	~300mJ
Pulse repetition frequency	30 Hz
exit beam diameter	13 cm
exit beam divergence	~0.1 mrad
pulse width	~5 ns
Pulse generator	Stanford Research Systems
Receiver	
Telescope diameter, f#, manufacturer	61 cm, f/9.3, Optical Guidance Systems
Wide FOV	2 mrad
Narrow FOV	0.3 mrad

Interference filters	See Table 2
Detectors	Photomultiplier tubes, electron tubes (9954B)
HV supplies	LeCroy
Data acquisition	Licel data recorders. Simultaneous photon counting and analog voltage measurement
raw data resolution	10s, 7.5m

### 4.3 Eye Safety

Eye-safety hazards exist inside the lidar enclosure when the laser is operating. The Nd:YAG lasers used in the Raman lidars are Class IV high-power laser transmitters. Precautions must be taken to prevent accidental exposure to both direct and reflected beams. Diffuse as well as specular beam reflections can cause severe eye and skin damage. As a result, access to the lidar enclosure is controlled by a safety interlock system, and only authorized personnel with appropriate eye protection are permitted entry.

From an operational point of view, we are most concerned with the characteristics of the laser beam once it leaves the enclosure. Before exiting the enclosure, the laser beam is expanded to 13 cm. Given that value and the other laser specifications, the maximum permissible exposure (MPE) for a single (5 ns) laser shot exiting the enclosure is given by

$$\text{MPE} = 4.71 \times 10^{-3} \text{ J/cm}^2 \text{ (ANSI Z136.1-2007)}$$

This is the maximum intensity for a single laser shot to be considered eye-safe according to the American National Standards Institute (ANSI). For the RL, the beam entering the atmosphere has a diameter of 13 cm (area =  $132.7 \text{ cm}^2$ ) and a pulse energy of less than 400 mJ. The pulse intensity exiting the enclosure is less than  $0.4 \text{ J} / 132.7 \text{ cm}^2 = 3.01 \times 10^{-3} \text{ J/cm}^2$ , which is smaller than the ANSI MPE value, and hence the system is considered eye-safe for exposure to a single laser shot. However, the MPE could potentially be exceeded with exposure to multiple shots.

Because the laser beam is transmitted vertically out of the enclosure, the eye-safety hazard that must be considered is to aircraft flying over the enclosure. Since a single pulse is eye-safe, the question then becomes: what is the likelihood of an aircraft being exposed to multiple pulses? Given the pulse repetition frequency of the lidar (30 Hz), calculations indicate that an aircraft would have to be flying less than  $5 \text{ ms}^{-1}$  immediately above the enclosure for any point on the aircraft to be exposed to multiple pulses. Since such a scenario is unlikely, the ARM RLs are considered eye-safe given the way they are operated.

### 4.4 Calibration

The raw return signals do not require calibration per se. However, derived quantities such as water vapor mixing ratio, temperature, and aerosol optical properties require careful calibration. The calibration procedures for these quantities are described in the VAP documentation (Newsom et al. 2019, 2020, Chand et al. 2020).

## 5.0 Data Description

### 5.1 Raw Data Collection and Ingest

Raw RL data packets are transmitted to the ARM Data Center (ADC) every 15 minutes. The ingest at the ADC then reformats these packets and appends them to the most recent file. Currently, the ingest is set up to generate two raw data files per day, with the first file covering the “AM” period from 0 to 12 (UTC) and the second file covering the “PM” period. Available datastreams include sgprlC1.a0 from RL01, twprlC3.a0 and enarlC1.a0 from RL02, and olirlM1.a0 from RL03. We note that the data format is the same for all three ARM RLs.

### 5.2 Raw Data File Contents

Each of the nine detection channels produce two signals (photon counts and analog voltages) that are logged by the data system. The data system records these signals with a time resolution of 10 s, and a range resolution of 7.5 m. The pre-pulse and backscatter signals are recorded with 4000 samples in the NFOV channels, and with 1500 samples in the wide-field-of-view (WFOV) channels. As a result, the NFOV channels are sampled out to a maximum range of about 27 km, and the WFOV channels are sampled out to about 8 km. The first ~400 samples of each profile occur before the pulse leaves the transceiver. This portion of the profile is used to establish solar background levels and analog voltage biases.

Table 4 lists the primary variables in the <site>rl<facility>.a0 datastream. The primary variables include the time and height arrays (for both FOVs), as well as 18 two-dimensional arrays of lidar return data from the nine detection channels. We note that photon counts and analog voltages are stored as integers. The analog voltage data in these files require conversion to floating point values with physical units (e.g., millivolts), as explained in Newsom et al. 2017. Also, the photon counting data are uncorrected for pulse pileup effects. These corrections are applied by the MERGE VAP (Newsom et al. 2017).

**Table 4.** Primary variables <site>rl<facility>.a0 datastream. Photon counts and analog voltages are stored as 2-dimensional arrays, where the two dimensions are time and height.

Variable	Description
base_time	File start time in seconds since 0 UTC on 1 Jan 1970.
time_offset	Time offset from begin of file in seconds
Water_counts_high	NFOV H2O Photon-counts
Water_analog_high	NFOV H2O Analog voltage
nitrogen_counts_high	NFOV N2 Photon-counts
nitrogen_analog_high	NFOV N2 Analog voltage
Elastic_counts_high	NFOV copol Photon-counts
Elastic_analog_high	NFOV copol Analog voltage
depolarization_counts_high	NFOV depol Photo-counts

Variable	Description
depolarization_analog_high	NFOV depol Analog voltage
t1_counts_high	NFOV RR1 Photo-counts
t1_analog_high	NFOV RR1 Analog voltage
t2_counts_high	NFOV RR2 Photo-counts
t2_analog_high	NFOV RR2 Analog voltage
Water_counts_low	WFOV H2O Photo-counts
Water_analog_low	NFOV H2O Analog voltage
nitrogen_counts_low	WFOV N2 Photo-counts
nitrogen_analog_low	WFOV N2 Analog voltage
Elastic_counts_low	WFOV unpol Photo-counts
Elastic_analog_low	WFOV unpol Analog voltage

The height resolution is stored as a global attribute call “vertical\_resolution\_high\_channels”. The data system starts recording a pulse several microseconds before the pulse leaves the enclosure. Determination of the height array requires determination of the height bin corresponding to the time when the pulse leaves the enclosure, which we refer to as the “ground bin.” The RLs are set up to record about 300 to 400 samples of the pre-pulse signal. The precise values of the “ground\_bin” are determined for each system through offline analysis and stored in a configuration file for use by the MERGE VAP (Newsom et al. 2018).

Table 5 lists the secondary variables in the <site>rl<facility>.a0 datastream. These include the number of laser pulses averaged, laser pulse energy, and the filter mode. The variable called “filter” is a flag indicating the filter wheel position, which is no longer used in the current design. With the current design of the system, a “filter” value of 1 or 2 indicates an open aperture, and a value of 0 indicates a closed aperture.

**Table 5.** Secondary variables in the <site>rl<facility>.a0 datastream.

Variable	Description
shots_summed_water_high	Number of laser shots accumulated for the water_high channel
shots_summed_nitrogen_high	Number of laser shots accumulated for the nitrogen_high channel
shots_summed_elastic_high	Number of laser shots accumulated for the elastic_high channel
shots_summed_depolarization_high	Number of laser shots accumulated for the depolarization_high channel
shots_summed_t1_high	Number of laser shots accumulated for the T1_high channel
shots_summed_t2_high	Number of laser shots accumulated for the T2_high channel
shots_summed_water_low	Number of laser shots accumulated for the water_low channel
shots_summed_nitrogen_low	Number of laser shots accumulated for the nitrogen_low channel
shots_summed_elastic_low	Number of laser shots accumulated for the elastic_low channel

Variable	Description
pulse_energy	Laser pulse energy in mJ
Filter	Flag indicating the filters currently in use. <ul style="list-style-type: none"> <li>• A value of 0 implies the filter wheels are closed.</li> <li>• A value of 1 implies that the common filter wheels are open and the LW channel has filter #1 in place.</li> <li>• A value of 2 implies that the common filter wheels are open and the LW channel has filter #2 in place.</li> </ul>

Table 6 lists the engineering and diagnostic variables in the raw RL datastream (<site>rl<facility>.a0). These variables provide information on the health of the system but are not used in the generation of any value-added-products. These variables include thermocouple measurements at various locations inside the RL trailer, as well as signals from the alignment module.

**Table 6.** Engineering and diagnostic variables in the raw RL datastream that provide information on the health of the system. They are not used in any of RL VAPs.

Variable	Description
n2_cloud_check_value	The sum of the nitrogen_high photon counting signal from 1.9-2.4 km normalized by the number of shots and the pulse energy. Used to determine cloud_value_check
cloud_value_check	A flag indicating cloudiness
laser_head	Laser head in use. 0 front, 1 rear
rh	Relative humidity inside the trailer
temp1 – temp6	Temperatures at various positions inside the trailer
s1 – s3	Temperatures at various positions inside the trailer
s4 – s8	Alignment module signals
s9 - s10	spares

### 5.3 Measurement Uncertainty

The raw signals acquired by the ARM RL are either photon counts or PMT analog voltages. These signals are assumed to obey Poisson statistics, such that the uncertainty in either the observed photon counts or analog voltage is given by the square root of that quantity. Further details on how these uncertainties are propagated in the RL VAPs are provided by Newsom et al. 2017, 2018.

### 5.4 Value-Added Products

Figure 14 shows a flow diagram of the current RL data processing procedure used by the ADC. Raw measurements from the <site>rl<facility>.a0 datastream are first processed by MERGE (Newsom et al. 2017). The MERGE VAP and radiosonde data are used as inputs to the Aerosol/Cloud process (Chand et al. 2019), and the water vapor mixing ratio (WVMR) and temperature calibration procedure (Newsom et al. 2018).

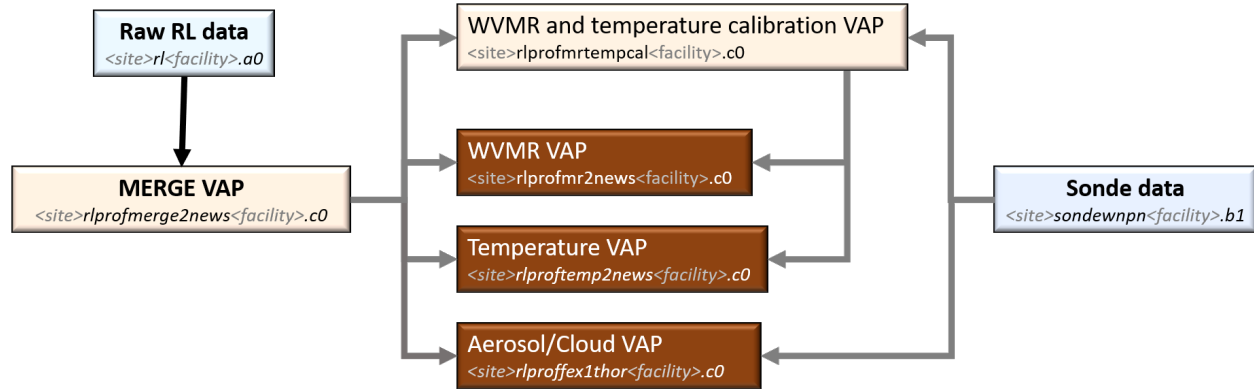


**Figure 14.** SGPRL VAP flow diagram. The inputs (light blue) to the overall data processing scheme include the raw RL data from the <site>rl<facility>.a0 datastream, and the radiosonde data from the <site>sondewnpn<facility>.b1. Intermediate data products (light yellow/tan) include the MERGE and WVMR and temperature calibration VAPs. The final (end-user) data products are highlighted a darker rust color.

Table 7 lists the various data products that are currently available from the RL through the ARM Data Discovery tool (<https://adc.arm.gov/discovery/>). Also shown are the ARM technical report numbers that document the corresponding data products. We refer the reader to these documents for data processing details associated with the various RL VAPs.

**Table 7.** Current RL value-added products.

Data Product	Level	Description	ARM Technical Report Number
rl	a0	Photon counts and analog voltages from each of the nine detection channels	DOE/SC-ARM-TR-038 (this report)
rlprofmerge2news	c0	Photon counting rates for each detection channel (from gluing photon counts and analog voltages)	DOE/SC-ARM-TR-189
rlprofmrtempcal	c0	Calibration data used by mixing ratio and temperature VAPs	DOE/SC-ARM-TR-218
rlprofmr2news10m	c0	Water vapor mixing ratio profiles at 10-minute resolution	DOE/SC-ARM-TR-218
rlproftemp2news10m	c0	Temperature profiles at 10-minute resolution	DOE/SC-ARM-TR-218
rlproffex1thor	c0	Aerosol scattering ratio, backscatter, extinction, lidar ratio, cloud mask, and depolarization ratio	DOE/SC-ARM-TR-224

## 5.5 Annotated Examples

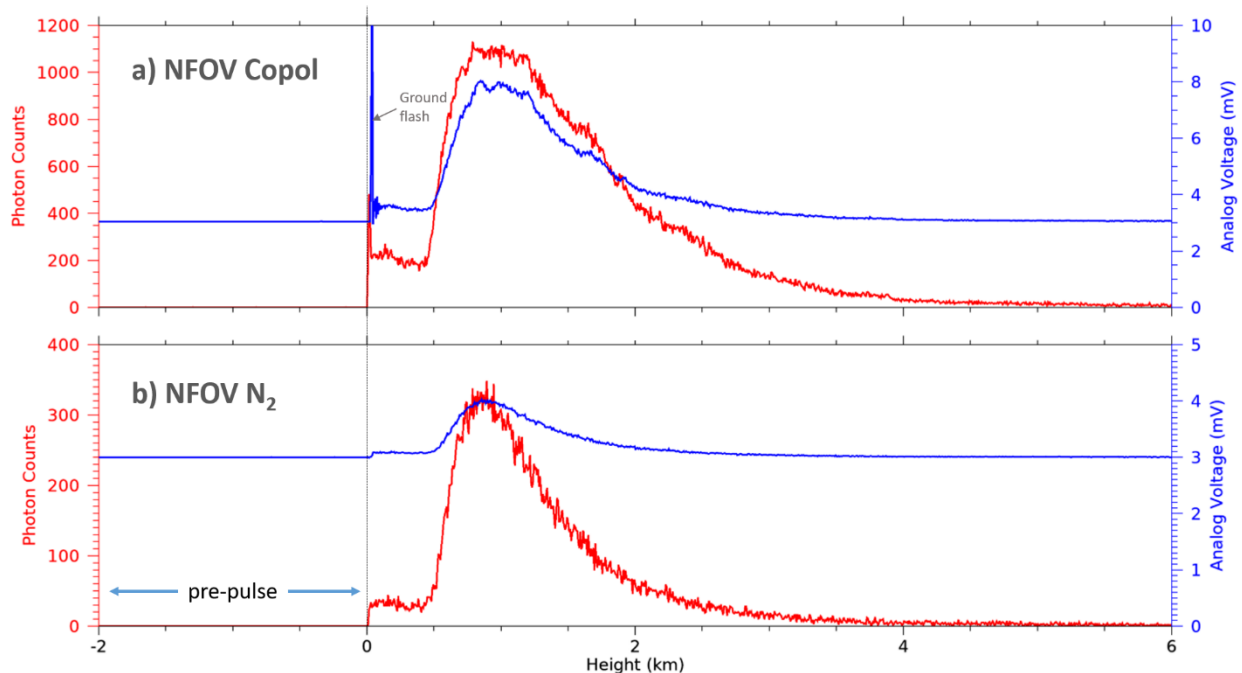
Figure 15 shows examples of typical return signals recorded by the RL01 under clear-sky conditions. This figure compares the signals from an elastic channel (NFOV Copol, in Figure 15a) to the signals from a

Raman channel (NFOV N2 in Figure 15b). The ground bin in this case was 327, which corresponds to the number of range bins in the pre-pulse part of the signal. Note that the ground bin exhibits a prominent spike in the elastic data but not in the N<sub>2</sub> data. This spike is the result of multiple scattered photons entering the receiver following a strong initial ground reflection as the pulse leaves the lidar.

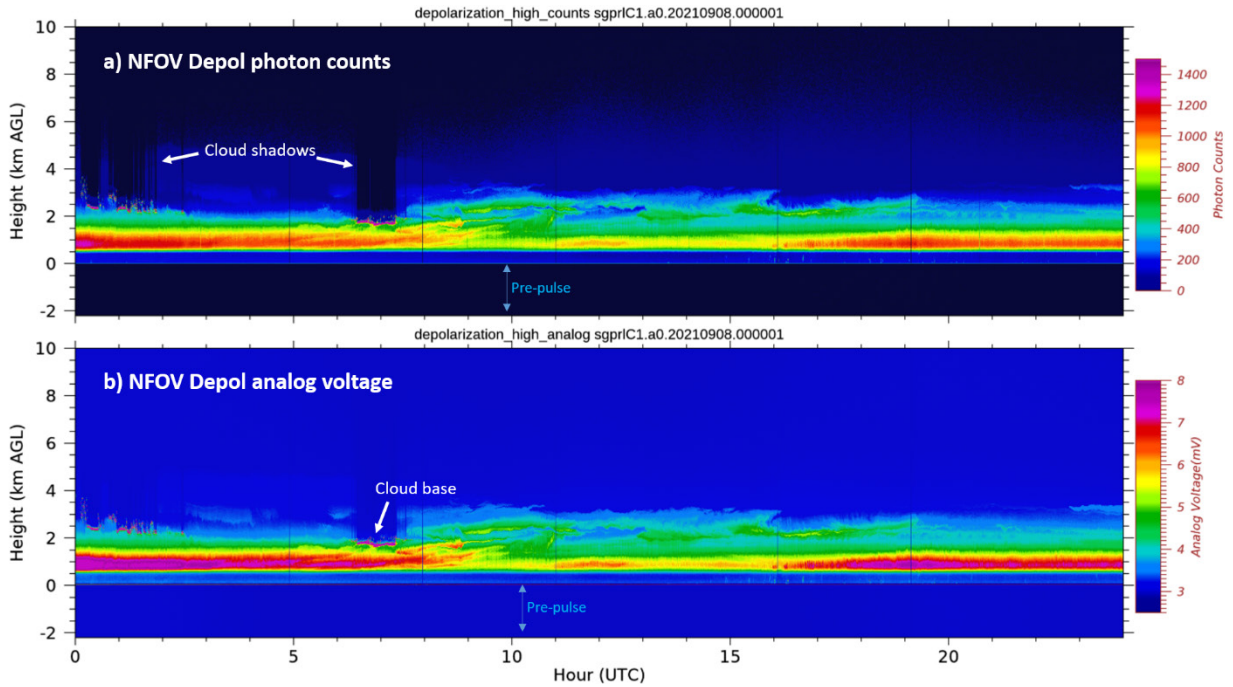
Figure 15 also shows that the raw analog voltages contain a DC offset. For a given channel, the offset is fixed, but different channels exhibit slightly different values for the offset. Generally, the offsets are in the range from 2 to 4 mV. We also note that there is a short delay in the analog signal relative to the photon counting signal.

Figure 16 through Figure 21 show sample time-height display of photon counts and analog voltages from all NFOV channels. These examples were taken from the RL01 at SGP C1 on 8 September 2021. Conditions were mostly clear but with some brief periods of cloudiness during the nighttime hours. We note that the nighttime period runs from about 00:30 UTC to 13:00 UTC.

Figure 22 and Figure 23 show comparisons between wide and narrow FOV measurements. Figure 22 shows a comparison between wide and narrow FOV N<sub>2</sub> channels. Similarly, Figure 23 shows a comparison between wide and narrow FOV H<sub>2</sub>O channels. The WFOV signals achieve their maxima at much lower altitudes than the NFOV signals. The WFOV signals also achieve complete overlap at much lower altitudes than the NFOV channels (~800 m versus ~4 km). Also, the figures show clearly that the WFOV channels are far more sensitive to solar radiation, as indicated by the high backgrounds.



**Figure 15.** Profiles of a) NFOV copol, and b) NFOV N<sub>2</sub>. The first ~300 range bins contain the pre-pulse signal. The range bin corresponding to  $z=0$  is identified by the strong ground return in the elastic signal. The analog signal contains a voltage bias, and is delayed relative to the photon-counting signal by several nanoseconds.



**Figure 16.** Sample time-height display of the NFOV Depol signals showing a) photon counts, and b) analog voltages. This example was taken from the RL01 (SGP C1) on 8 September 2021.

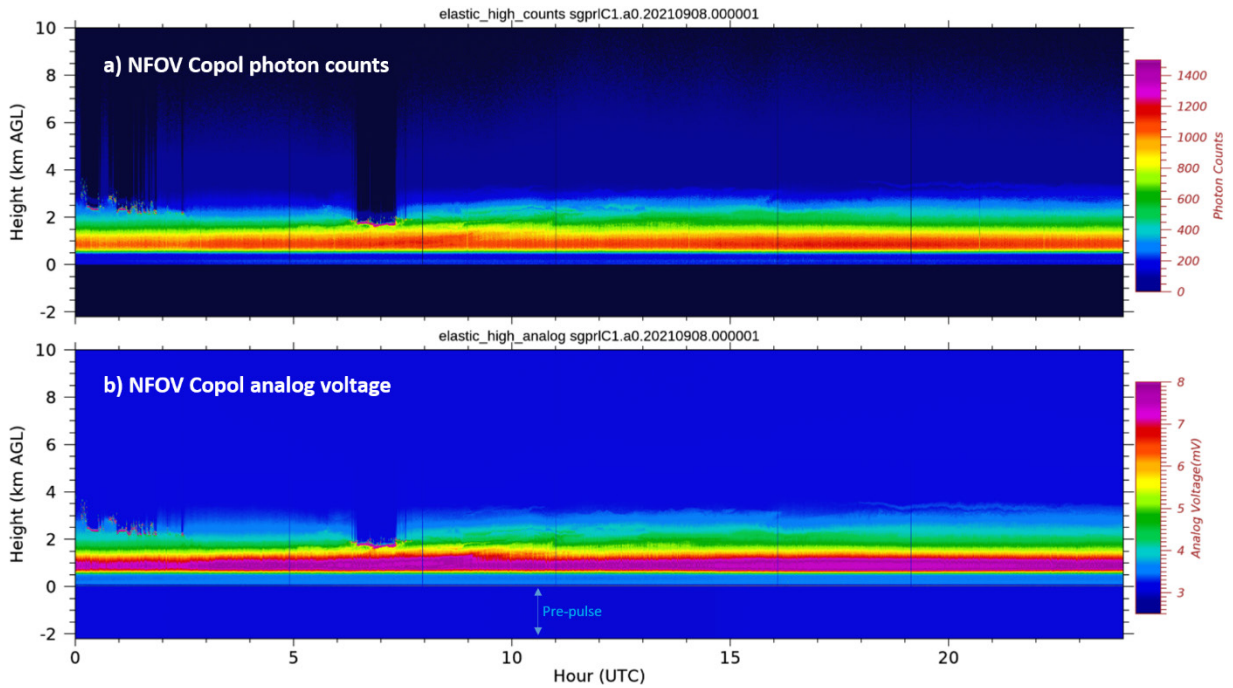


**Figure 17.** Sample time-height display of the NFOV Copol signals showing a) photon counts, and b) analog voltages. This example was taken from the RL01 (SGP C1) on 8 September 2021.

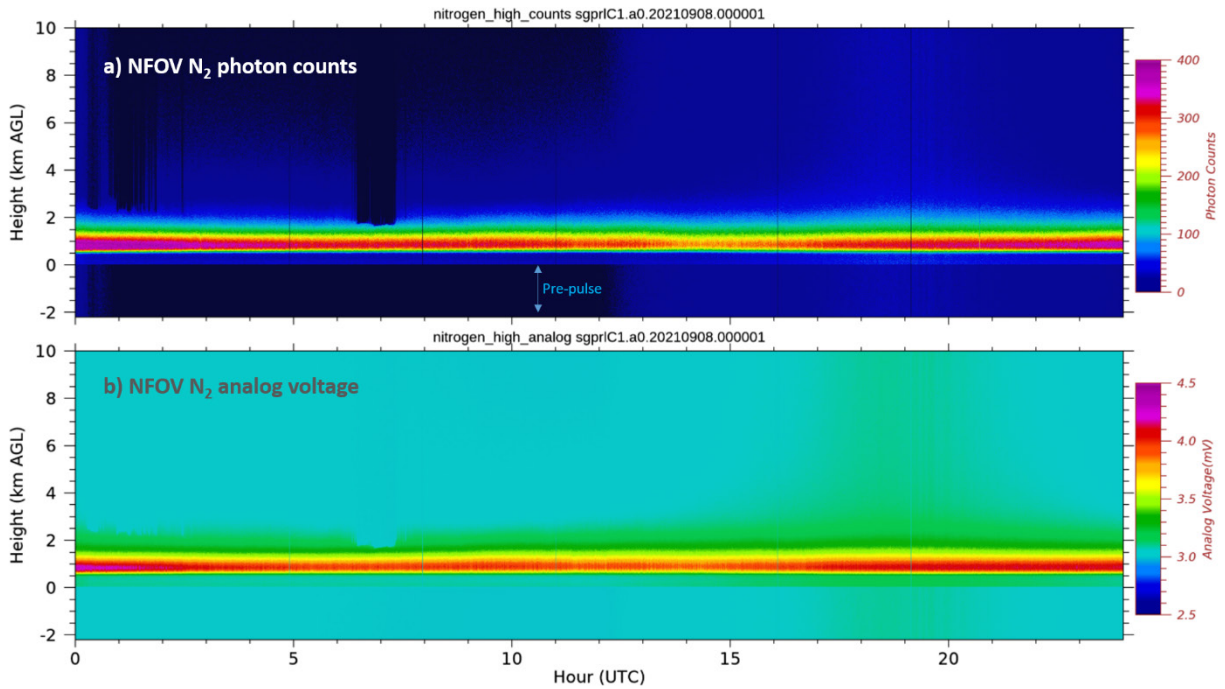


**Figure 18.** Sample time-height display of the NFOV  $N_2$  signals showing a) photon counts, and b) analog voltages. This example was taken from the RL01 (SGP C1) on 8 September 2021.

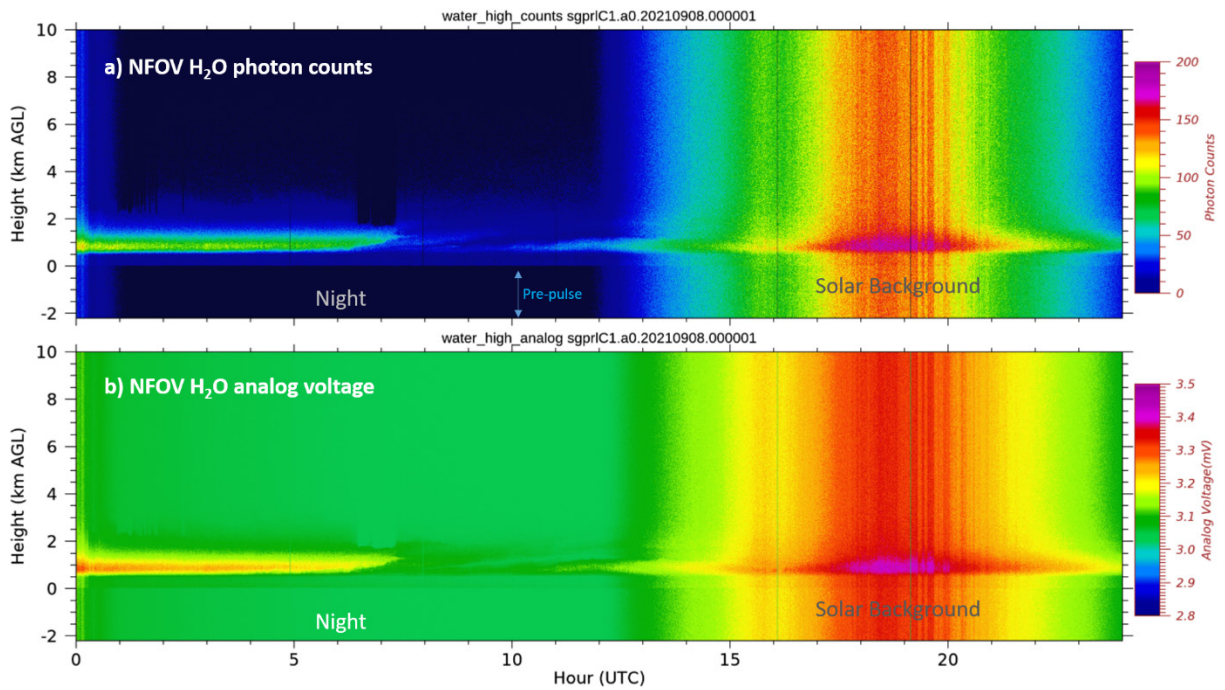


**Figure 19.** Sample time-height display of the NFOV  $H_2O$  signals showing a) photon counts, and b) analog voltages. This example was taken from the RL01 (SGP C1) on 8 September 2021.

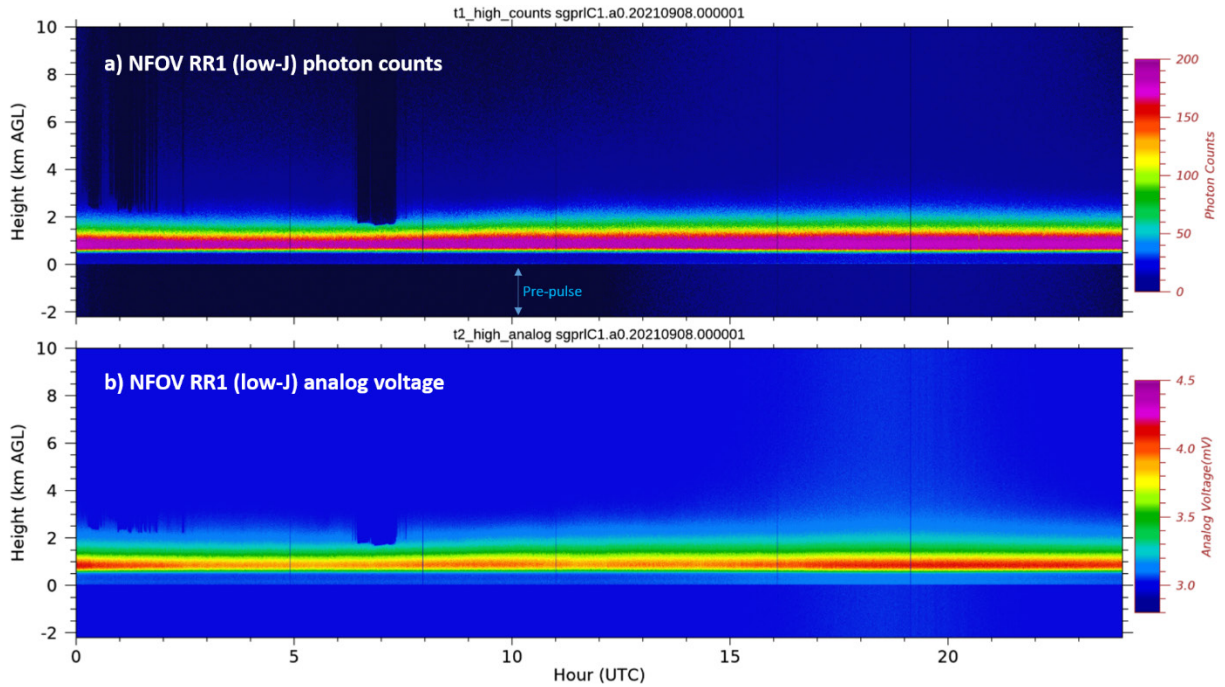


**Figure 20.** Sample time-height display of the NFOV RR1 signals showing a) photon counts, and b) analog voltages. This example was taken from the RL01 (SGP C1) on 8 September 2021.

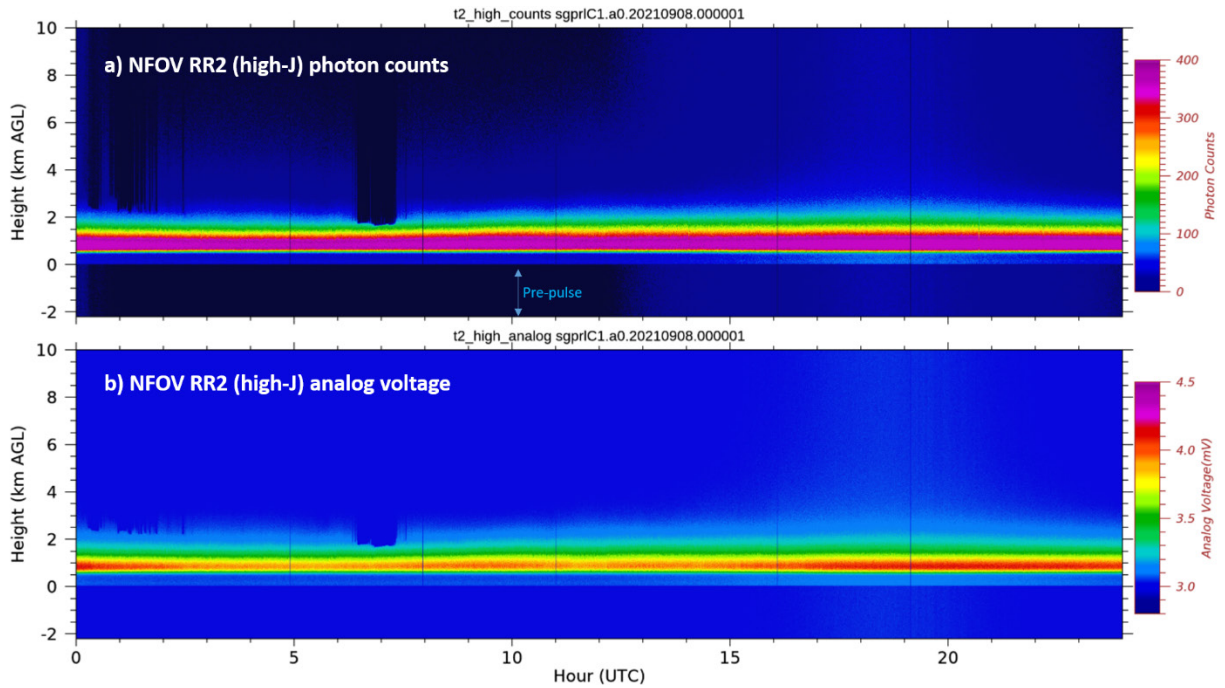


**Figure 21.** Sample time-height display of the NFOV RR2 signals showing a) photon counts, and b) analog voltages. This example was taken from the RL01 (SGP C1) on 8 September 2021.

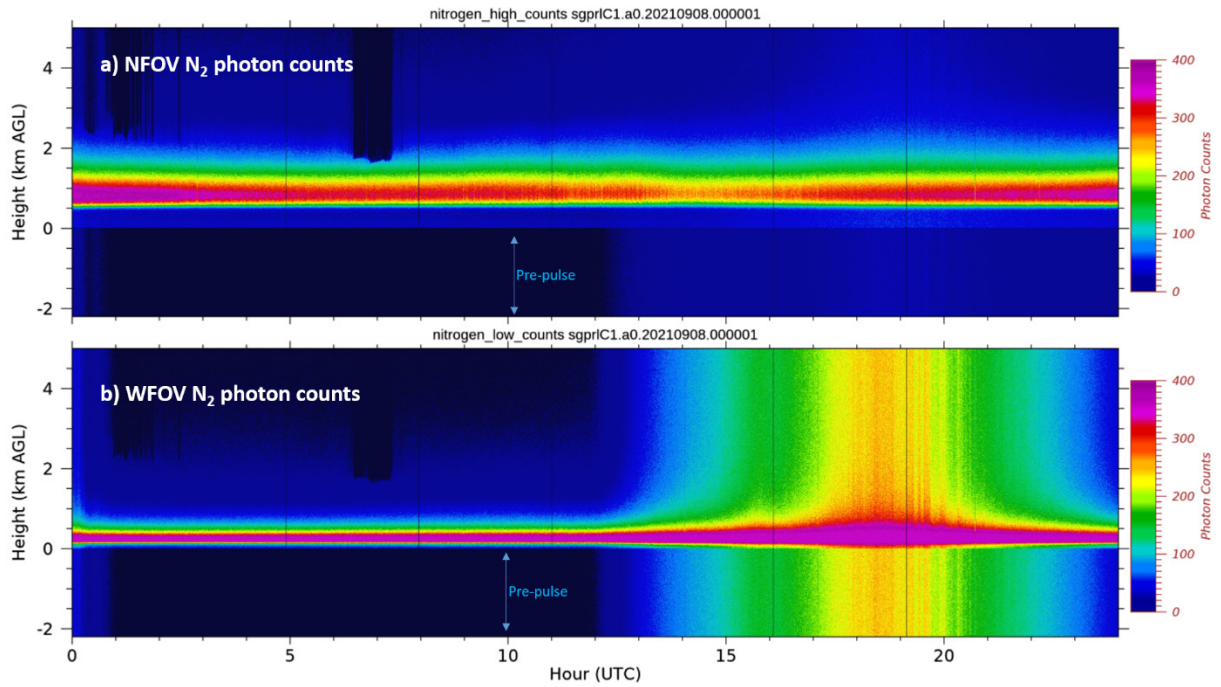


**Figure 22.** Comparison of the a) NFOV and b) WFOV photon counting signal for N<sub>2</sub>. This example was taken from the RL01 (SGP C1) on 8 September 2021.

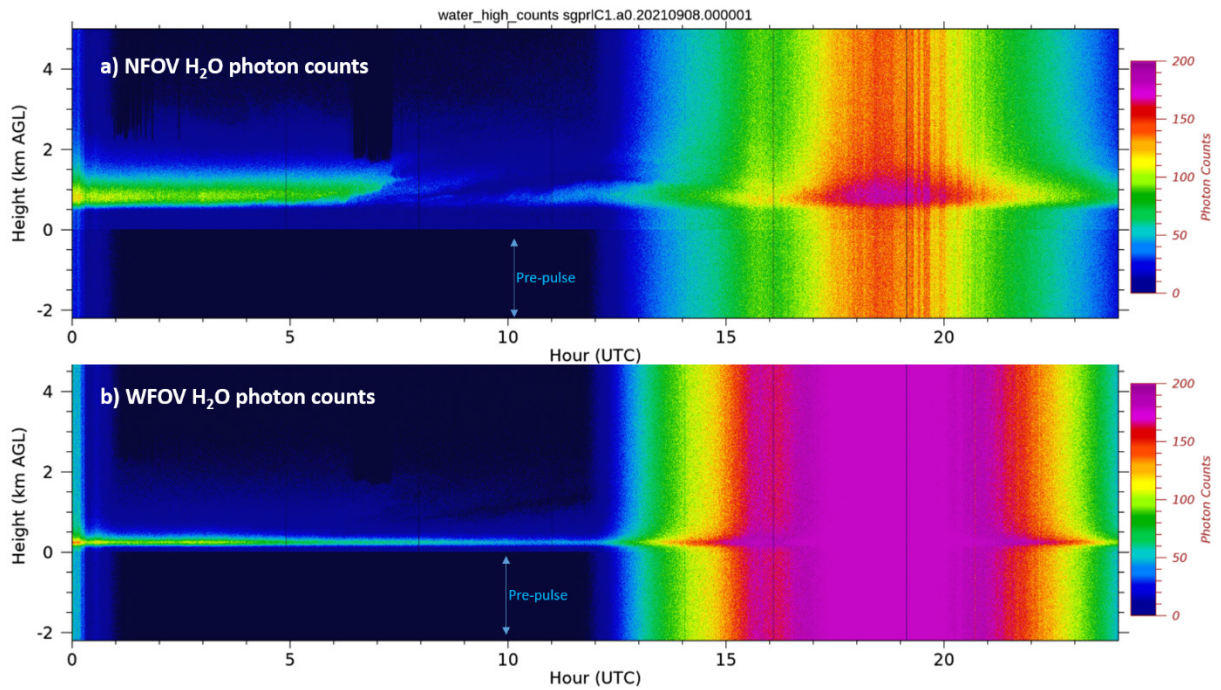


**Figure 23.** Comparison of the a) NFOV and b) WFOV photon counting signals for H<sub>2</sub>O. This example was taken from the RL01 (SGP C1) on 8 September 2021.

## 6.0 References

[ANSI Z136.1-2007](#). “American National Standard for Safe Use of Lasers”, Table 5a, pp. 74.

Chand, D, RK Newsom, T Thorsen, E Cromwell, C Sivaraman, C Flynn, J Shilling, and J Comstock. 2019. Aerosol and Cloud Optical Properties from the ARM Raman Lidars: The Feature Detection and Extinction (FEX) Value-Added Product. U.S. Department of Energy, Atmospheric Radiation Measurement user facility, Richland, Washington. DOE/SC-ARM/TR-218, [doi:10.2172/1489497](https://doi.org/10.2172/1489497)

Ferrare, RA, DD Turner, M Clayton, B Schmid, J Redemann, D Covert, R Elleman, J Ogren, E Andrews, JEM Goldsmith, and H Jonsson. 2006. “Evaluation of daytime measurements of aerosols and water vapor made by an operational Raman lidar over the Southern Great Plains.” *Journal of Geophysical Research – Atmospheres* 111(D5): D05S08, <https://doi.org/10.1029/2005JD005836>

Goldsmith, JEM, FH Blair, SE Bisson, and DD Turner. 1998. “Turn-key Raman lidar for profiling atmospheric water vapor, clouds, and aerosols.” *Applied Optics* 37(21): 4979–4990, <https://doi.org/10.1364/AO.37.004979>

Mather, JH, and JW Voyles. 2013. “The Arm Climate Research Facility: A Review of Structure and Capabilities.” *Bulletin of the American Meteorological Society* 94(3): 377–392, <https://doi.org/10.1175/BAMS-D-11-00218.1>

Newsom, RK, DD Turner, B Mielke, M Clayton, RA Ferrare, and C Sivaraman. 2009. “Use of Simultaneous analog and photon counting detection for Raman Lidar.” *Applied Optics* 48(20): 3903–3914, <https://doi.org/10.1364/AO.48.003903>

Newsom, RK, DD Turner, and JEM Goldsmith. 2013. “Long-term evaluation of temperature profiles measured by an operational Raman lidar.” *Journal of Atmospheric and Oceanic Technology* 30(8): 1616–1634, <https://doi.org/10.1175/JTECH-D-12-00138.1>

Newsom RK, J Goldsmith, and C Sivaraman. 2017. Raman Lidar MERGE Value-Added Product. U.S. Department of Energy, Atmospheric Radiation Measurement user facility, Richland, Washington. DOE/SC-ARM-TR-189, [doi:10.2172/1353443](https://doi.org/10.2172/1353443)

Newsom RK, C Sivaraman. 2018. Raman Lidar Water Vapor Mixing Ratio and Temperature Value-Added Products. U.S. Department of Energy, Atmospheric Radiation user facility, Richland, Washington. DOE/SC-ARM/TR-218, [doi:10.2172/1489497](https://doi.org/10.2172/1489497)

Raman, CV. 1928. “A new radiation.” *Indian Journal of Physics* 2: 387–398. [hdl:10821/377](https://doi.org/10.10821/377)

Stokes GM, and SE Schwartz. 1994. “The Atmospheric Radiation Measurement (ARM) Program: Programmatic background and design of the Cloud and Radiation Test Bed.” *Bulletin of the American Meteorological Society* 75(7): 1201–1222, [https://doi.org/10.1175/1520-0477\(1994\)075<1201:TARMPP>2.0.CO;2](https://doi.org/10.1175/1520-0477(1994)075<1201:TARMPP>2.0.CO;2)

Thorsen, TJ, Q Fu, RK Newsom, DD Turner, and JM Comstock. 2015a. “Automated retrieval of cloud and aerosol properties from the ARM Raman lidar. Part I: Feature detection.” *Journal of Atmospheric and Oceanic Technology* 32(11): 1977–1998, <https://doi.org/10.1175/JTECH-D-14-00150.1>

Thorsen, TJ, and Q Fu. 2015b. “Automated retrieval of cloud and aerosol properties from the ARM Raman lidar. Part II: Extinction.” *Journal of Atmospheric and Oceanic Technology* 32(11): 1999–2023, <https://doi.org/10.1175/JTECH-D-14-00178.1>

Turner, DD, and JEM Goldsmith. 1999. “Twenty-four-hour Raman lidar water vapor measurements during the Atmospheric Radiation Measurement Program’s 1996 and 1997 water vapor intensive observation periods.” *Journal of Atmospheric and Oceanic Technology* 16(8): 1062–1076, [https://doi.org/10.1175/1520-0426\(1999\)016<1062:TFHRLW>2.0.CO;2](https://doi.org/10.1175/1520-0426(1999)016<1062:TFHRLW>2.0.CO;2)

Turner, DD, WF Feltz, and RA Ferrare. 2000. “Continuous water vapor profiles from operational active and passive remote sensors.” *Bulletin of the American Meteorological Society* 81(6): 1301–1317, [https://doi.org/10.1175/1520-0477\(2000\)081<1301:CWBPF0>2.3.CO;2](https://doi.org/10.1175/1520-0477(2000)081<1301:CWBPF0>2.3.CO;2)

Turner DD, RA Ferrare, LA Heilman Brasseur, WF Feltz, and TP Tooman. 2002. “Automated retrievals of water vapor and aerosol profiles from an operational Raman lidar.” *Journal of Atmospheric and Oceanic Technology* 19(1): 37–50, [https://doi.org/10.1175/1520-0426\(2002\)019<0037:AROWVA>2.0.CO;2](https://doi.org/10.1175/1520-0426(2002)019<0037:AROWVA>2.0.CO;2)

Turner, DD, and JEM Goldsmith. 2005. “[The refurbishment and upgrade of the Atmospheric Radiation Measurement Raman lidar](#).” Fifteenth ARM Science Team Meeting Proceedings, U.S. Department of Energy, Atmospheric Radiation Measurement user facility, Richland, Washington.

Turner, DD, JEM Goldsmith, and RA Ferrare. 2016. “Development and applications of the ARM Raman lidar.” *The Atmospheric Radiation Measurement Program: The First 20 Years. American Meteorological Society Meteorological Monograph* 57: 18.1–18.15, <https://doi.org/10.1175/AMSMONOGRAPHS-D-15-0026.1>

Whiteman, DN, SH Melfi, and RA Ferrare. 1992. “Raman lidar system for the measurement of water vapor and aerosols in the Earth’s atmosphere.” *Applied Optics* 31(16): 3068–3082, <https://doi.org/10.1364/AO.31.003068>

Whiteman, DN, B Demoz, P Di Girolamo, J Comer, I Veselovskii, K Evans, Z Wang, M Cadirola, K Rush, G Schwemmer, B Gentry, SH Melfi, B Mielke, D Venable, and T Van Hove. 2006. “Raman Water Vapor Lidar Measurements during the International H<sub>2</sub>O Project. Part I: Instrumentation and Analysis Techniques.” *Journal of Atmospheric and Oceanic Technology* 23(2): 157–169, <https://doi.org/10.1175/JTECH1838.1>



U.S. DEPARTMENT OF  
**ENERGY**

---

Office of Science